

Preparation of a Hybrid TiO₂ and 1T/2H-MoS₂ Photocatalyst for the Degradation of Tetracycline Hydrochloride

Miaogen Chen,* Wenya Chang, Jing Zhang, Wan Zhao, and Zhi Chen*



Cite This: *ACS Omega* 2023, 8, 15458–15466

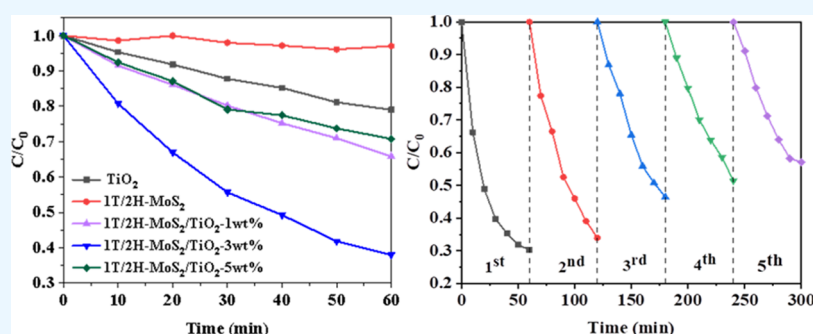


Read Online

ACCESS |

Metrics & More

Article Recommendations



ABSTRACT: Water pollution caused by antibiotics is a growing problem. Semiconductor photocatalysis is an environmentally friendly technology that can effectively degrade organic pollutants in water. Therefore, the development of efficient photocatalysts is of great significance to solve the environmental pollution problem. In this paper, mixed-phase TiO₂ and 1T/2H-MoS₂ composite (1T/2H-MoS₂/TiO₂) were synthesized by the in situ growth method. The prepared compounds were characterized and applied to the visible-light degradation of tetracycline hydrochloride. The photocatalytic effect of 1T/2H-MoS₂/TiO₂ on tetracycline hydrochloride is significantly enhanced under visible light and has good stability. It has potential applications in the treatment of organic pollutants in water.

1. INTRODUCTION

In modern society, water pollution due to heavy metals and organic pollutants has become more serious. Nowadays, antibiotics are abused by humans and continuously discharged into the surface water or groundwater environment, causing a series of water pollution problems.^{1–3} Semiconductor photocatalysis is a green and efficient technology for treating antibiotic contaminants in water by converting solar energy into chemical energy and mineralizing organic matter without creating secondary pollution.⁴ The core of photocatalysis technology is the development of superior-performance photocatalysts. Titanium dioxide (TiO₂) is one of the most researched photocatalyst materials.^{5,6} Many phases of TiO₂ have been widely applied and extensively researched, such as commercial TiO₂ P₂₅ and rutile TiO₂.⁷ TiO₂ catalysts with anatase phase suffer from low utilization of sunlight and low carrier separation efficiency, limiting their industrial applications.⁸ Compared with anatase TiO₂, the unique crystal phase configuration of mixed-phase TiO₂ improves the separation efficiency of photogenerated carrier and thus has better photocatalytic activity.⁹

Constructing heterojunction is an effective method to broaden the absorption spectrum and improve the carrier separation efficiency. The materials currently used to construct

heterojunctions with TiO₂ can be broadly classified into two main categories: noble metals and semiconductor oxides.¹⁰ Modification of TiO₂ with noble metals can largely facilitate carrier separation while broadening its photoresponse range and improving its sensitivity to visible radiation. However, the high cost of using precious metals to modify TiO₂ has limited its large-scale application in the industry. Therefore, the search for materials that can replace noble metals is an urgent issue to be addressed. Molybdenum disulfide (MoS₂) is a new type of semiconductor photocatalyst that has received widespread attention for its unique structure and excellent photovoltaic properties.¹¹ MoS₂ has a two-dimensional layer-like structure similar to graphene, with a single layer consisting of two layers of S atoms and a layer of Mo atoms sandwiched in between.¹² MoS₂ has two common crystal structures, namely, 2H-MoS₂ and 1T-MoS₂, among which 2H-MoS₂ is a relatively stable semiconductor phase molybdenum disulfide existing in nature,

Received: February 3, 2023

Accepted: April 11, 2023

Published: April 21, 2023



with two layers of a unit cell and a hexagonal crystal structure; 1T-MoS₂ is an artificially produced metallic phase molybdenum disulfide with only one layer of a unit cell and a tetragonal crystal structure.^{13–15} Compared with 2H-MoS₂, 1T-MoS₂ has more active sites and higher electronic conductivity.¹⁶ Bai et al. reported a hybridized 1T-2H-MoS₂/TiO₂ photocatalyst, showing that hybridized 1T-2H-MoS₂ provided a more efficient charge separation than a semiconducting 2H-MoS₂.¹⁷ Also, it is indicated that 1T-MoS₂ has higher activity than noble metal Pt and is a promising cocatalyst to replace the noble metal.¹⁸ Molybdenum disulfide (1T/2H-MoS₂), which coexists in a metal phase and a semiconductor phase, has two phase structures at the same time. It not only has good activity and charge transport performance of the metal phase but also has the stability of the semiconductor phase. It is an ideal cocatalyst material.¹⁹

In this work, mixed-phase TiO₂ was obtained by the sol–gel method, followed by the 1T/2H-MoS₂/TiO₂ composite prepared by the in situ growth method. The photocatalytic performance of the as-prepared 1T/2H-MoS₂/TiO₂ photocatalyst for the degradation of organic pollutants under visible light was evaluated. The results show that the 1T/2H-MoS₂/TiO₂ photocatalyst exhibits excellent photocatalytic activity. Also, its structure, properties, cyclic stability, and degradation mechanism were deeply explored.

2. EXPERIMENT

2.1. Materials. All of the reagents were used directly after being purchased. Anhydrous ethanol (C₂H₆O), Pluronic F127, tetrabutyl titanate (C₁₆H₃₆O₄Ti), molybdenum trioxide (MoO₃) were obtained from Shanghai Macklin Biochemical Technology Co. Ltd. (Shanghai, China). Thioacetamide (C₂H₅NS), urea (H₂NCONH₂), and tetracycline hydrochloride (C₂₂H₂₄N₂O₈·HCl, TC-HCl) were obtained from Shanghai Aladdin Biochemical Technology Co. Ltd. (Shanghai, China).

2.2. Preparation. *Preparation of TiO₂ Microspheres.* Add 1.5 g of Pluronic F127 into 35 mL of absolute ethanol, add 100 μL of deionized water at the same time, stir the mixture magnetically for 30 min, then add 3.4 mL of TBOT, and continue magnetic stirring for 12 h. The stirred product was centrifuged and washed twice with absolute ethanol. The washed solid matter was dried in a vacuum oven at 60 °C for 2 h. Then, the dried solid matter was placed in a muffle furnace and calcined at 500 °C for 2 h to obtain a white mixed-phase TiO₂ sample.

*Preparation of 1T/2H-MoS₂ Particles.*²⁰ Molybdenum trioxide (MoO₃, 0.096 g), 0.112 g of thioacetamide (TAA), involved in the synthesis of 1T/2H-MoS₂ samples as a reactant, and 0.96 g urea were dissolved in 80 mL of deionized water and magnetically stirred for 2 h to form a uniform 1T/2H-MoS₂ precursor solution. Then, the above solution was mixed and transferred to the reaction kettle, placed in a blast drying oven, reaction at 200 °C for 12 h. After the reaction was completed, the solid product was collected, washed three times with deionized water and anhydrous ethanol, and then placed in a vacuum drying oven at 60 °C for 12 h to obtain 1T/2H-MoS₂ samples.

Preparation of 1T/2H-MoS₂/TiO₂. Taking 1T/2H-MoS₂/TiO₂-3wt % as an example, 6 mg of MoO₃, 7 mg of TAA, and 0.06 g of urea were dissolved in 10 mL of deionized water and magnetically stirred for 1 h to form a uniform 1T/2H-MoS₂ precursor solution. Then, 0.222 g of TiO₂ and 30 mL of

deionized water were added to the 1T/2H-MoS₂ precursor solution. The mixture was continued to be magnetically stirred for 1 h to form a uniform suspension. The above suspension was transferred to an autoclave and placed in a blast drying oven at 200 °C for 12 h. After the reaction was complete, the products after the reaction were collected and washed three times by centrifugation with deionized water and anhydrous ethanol. By changing the amount of TiO₂ added or by the ratio of 1T/2H-MoS₂ precursor solution, 1T/2H-MoS₂/TiO₂ samples with different mass ratios can be obtained. After drying for 12 h in a vacuum oven at 60 °C, the 1T/2H-MoS₂/TiO₂ samples can be obtained.

2.3. Characterization. XRD (X-ray diffractometer) data were obtained from SmartLab (Rigaku) using Cu Kα line with step size 0.02°. XPS (X-ray photoelectron spectroscopy) was carried out on an ESCALAB 250Xi spectrometer (Thermo Scientific) using Al Kα X-ray (hν=1486.65 eV) as a source. FESEM (field emission scanning electron microscopy) was conducted on GeminiSEM (ZEISS, Germany). HRTEM (high-resolution transmission electron microscopy) images were observed by transmission electron microscopy (JEM 2100F) using ultrathin carbon film copper mesh at a 200 kV acceleration voltage. UV–vis DRS (ultraviolet–visible diffuse reflectance spectra) were obtained on a UV-3600Plus UV–vis spectrophotometer equipped with an integrating sphere attachment in the range of 200–800 nm.

2.4. Photoelectrochemical Measurements. Electrochemical tests were operated at the CHI660E electrochemical workstation. By using a standard three-electrode cell with a platinum wire as the counter electrode, a standard calomel electrode (SCE) as the reference electrode, and 30 mg of prepared TiO₂, 1T/2H-MoS₂ and 1T/2H-MoS₂/TiO₂ were separately dissolved in 3 mL of poly(vinylidene fluoride) (PVDF) solution and coated on the FTO conducting glass (1 cm × 2 cm) by spin coating to form the working electrode, respectively. Forty milliliters of Na₂SO₄ (0.5 M) was used as an electrolyte and a 300 W Xe lamp assembled with a cutoff filter (λ > 420 nm) was used as the light source.

2.5. Photocatalytic Performance. The photocatalytic activities of the prepared 1T/2H-MoS₂/TiO₂ were evaluated by the degradation of antibiotic (tetracycline hydrochloride, TC-HCl) in water. The photocatalytic analysis was operated at a constant temperature by a circulating cooling system. The prepared 1T/2H-MoS₂/TiO₂ was immersed in 100 mL of 20.0 mg/L TC-HCl solution. Before the light irradiation, the solution with the photocatalyst was magnetically stirred in darkness for 1 h to establish adsorption equilibrium. During the light irradiation, 5.0 mL of the solution was taken out every 10 min and centrifuged to separate the solid. The concentration of TC-HCl was investigated at its maximum adsorption of 356 nm on the UV 2600 spectrophotometer.

3. RESULTS AND DISCUSSION

The XRD diffractograms of 1T/2H-MoS₂, TiO₂, and 1T/2H-MoS₂/TiO₂ are shown in Figure 1. The black curve is the XRD diffractogram of the rutile-anatase mixed-phase TiO₂ with two distinct diffraction peaks at 25.3 and 27.4°. Upon comparison with the standard PDF cards (JCPDS: 71-1166, JCPDS: 76-1939), it can be seen that the two diffraction peaks correspond to the (1 0 1) crystal plane of anatase TiO₂ and the small peak near 11° can be attributed to TiO. The red curve in the figure shows the XRD diffraction pattern of 1T/2H-MoS₂ with a similar peak shape to that of 2H-MoS₂. A comparison with the

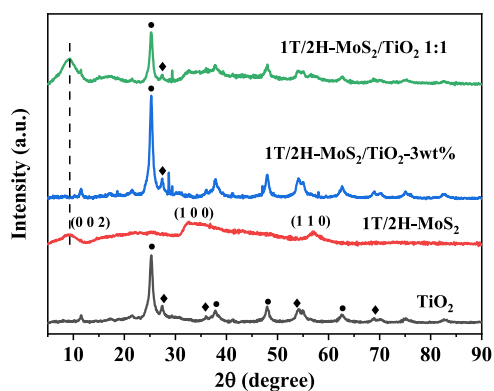


Figure 1. XRD plots of TiO_2 , $1\text{T}/2\text{H-MoS}_2$, and different ratios of $1\text{T}/2\text{H-MoS}_2/\text{TiO}_2$, with circles representing the anatase phase and diamonds representing the rutile phase.

PDF card of 2H-MoS_2 (JCPDS: 73-1508) shows that 2H-MoS_2 has a diffraction peak near 14.3° , corresponding to the (0 0 2) crystal plane, whereas $1\text{T}/2\text{H-MoS}_2$ has a diffraction peak at 9.8° corresponding to the (0 0 2) crystal plane, which, according to the previous literature, is the characteristic peak of 1T-MoS_2 .²¹ The change in the peak position may be due to the dominance of the octahedral structure of the 1T phase. The XRD diffraction pattern of $1\text{T}/2\text{H-MoS}_2/\text{TiO}_2\text{-3wt\%}$ shows the characteristic peaks of both phases of TiO_2 , proving that the preparation of the composite does not destroy the formation of the TiO_2 phase. Some spurious peaks can be observed near 28° , which were found to originate from incomplete MoO_3 upon comparison with the standard PDF card. The $1\text{T}/2\text{H-MoS}_2/\text{TiO}_2\text{-3wt\%}$ XRD diffraction pattern did not show obvious peaks of $1\text{T}/2\text{H-MoS}_2$. With increasing the proportion of $1\text{T}/2\text{H-MoS}_2$ in the composite, a clear peak of $1\text{T}/2\text{H-MoS}_2$ was observed in the $1\text{T}/2\text{H-MoS}_2/\text{TiO}_2$ 1:1 XRD diffractograms, which demonstrates the successful preparation of the $1\text{T}/2\text{H-MoS}_2/\text{TiO}_2$ composite photocatalyst.

The phase formation of the sample was further determined by Raman spectroscopy. As shown in Figure 2, another six obvious peaks appeared at 151, 195, 285, 335, and 376 cm^{-1} in the Raman image of $1\text{T}/2\text{H-MoS}_2$. The peaks at 151, 195, 285, and 335 cm^{-1} correspond to 1T-MoS_2 and can be attributed to the Mo–Mo stretching vibrations and phonon modes in 1T-

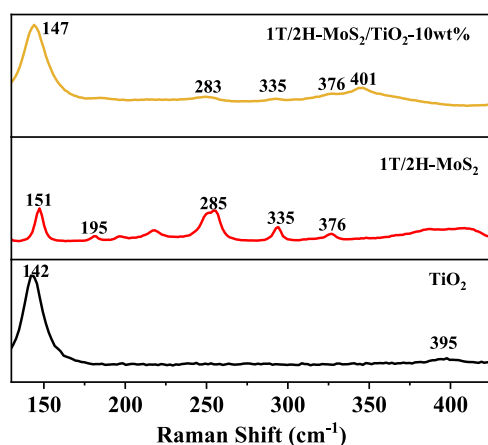


Figure 2. Raman spectra of TiO_2 , $1\text{T}/2\text{H-MoS}_2$, and $1\text{T}/2\text{H-MoS}_2/\text{TiO}_2\text{-10wt\%}$.

MoS_2 . The peak located at 376 cm^{-1} , on the other hand, is caused by 2 S atoms vibrating in opposite directions with respect to the Mo atom and belongs to the typical E_{2g}^1 vibrational mode of 2H-MoS_2 , which is consistent with the relevant findings of previous studies on 1T-MoS_2 and 2H-MoS_2 , thus allowing further determination of the successful preparation of $1\text{T}/2\text{H-MoS}_2$.²² In the Raman diagram of TiO_2 , two peaks at 142 and 395 cm^{-1} correspond to the characteristic peaks of the E_g and B_{1g} vibrational modes, respectively.²³ $1\text{T}/2\text{H-MoS}_2/\text{TiO}_2\text{-10wt\%}$ shows a new peak at 401 cm^{-1} , which can be attributed to the A_g^1 vibrational mode of 2H-MoS_2 , and another peak at 147, 283, 335, and 376 cm^{-1} can be observed as characteristic peaks belonging to each of TiO_2 and $1\text{T}/2\text{H-MoS}_2$, with a small displacement between the peak positions and those of the single sample. On the one hand, it can be shown that TiO_2 and $1\text{T}/2\text{H-MoS}_2$ coexist in the composite material, and their structures are not destroyed by the hydrothermal process. On the other hand, TiO_2 has valence bond interaction with $1\text{T}/2\text{H-MoS}_2$. On the other hand, it can be explained that there is a valence bond interaction between TiO_2 and $1\text{T}/2\text{H-MoS}_2$.

Figure 3a–c shows the SEM images of TiO_2 , $1\text{T}/2\text{H-MoS}_2$, and $1\text{T}/2\text{H-MoS}_2/\text{TiO}_2$, from which the morphology of the three samples can be observed. The elemental distribution of $1\text{T}/2\text{H-MoS}_2/\text{TiO}_2$ is shown in Figure 3d–i, which shows that Mo, S, Ti, and O elements are evenly distributed on the surface of $1\text{T}/2\text{H-MoS}_2/\text{TiO}_2$. The surface is more evenly distributed. The microstructures of TiO_2 , $1\text{T}/2\text{H-MoS}_2$, and $1\text{T}/2\text{H-MoS}_2/\text{TiO}_2$ were further observed by TEM. Figure 4a shows the high-resolution TEM image of TiO_2 , in which two sets of lattice stripes at 0.35 nm and 0.32 nm can be observed, corresponding to the (1 0 1) crystallographic plane of the anatase phase and the (1 1 0) crystallographic plane of the rutile phase,^{24,25} further demonstrating the successful preparation of the mixed-phase TiO_2 . Figure 4b,c shows the high-resolution TEM images of $1\text{T}/2\text{H-MoS}_2$, in which lattice stripes of 0.92 nm and 0.62 nm can be observed, corresponding to the (0 0 2) crystal plane of 1T-MoS_2 and the (0 0 2) crystal plane of 2H-MoS_2 , further confirming the coexistence of the 1T phase with the 2H phase. Figure 4d,e shows the high-resolution TEM images of $1\text{T}/2\text{H-MoS}_2/\text{TiO}_2$, where, in addition to the lattice stripes mentioned above, a lattice stripe of 0.297 nm can be observed, corresponding to the (1 0 0) crystallographic plane of 2H-MoS_2 .

Figure 5a shows the full XPS spectrum of $1\text{T}/2\text{H-MoS}_2/\text{TiO}_2$, from which it can be observed that the sample contains four elements, Mo, S, Ti, and O, which are consistent with the theoretical elements used to design the experiment. Figure 5b shows the fine spectrum of Ti 2p, from which two distinct characteristic peaks can be observed at 458.7 and 464.4 eV, corresponding to Ti $2p_{3/2}$ and Ti $2p_{1/2}$, attributed to Ti^{4+} .^{26,27} Figure 5c shows the fine spectrum of O 1s. The characteristic peaks located at 530.2 and 532.0 eV correspond to O–Ti and O–H bonds,²⁸ thus demonstrating the presence of TiO_2 in the composite photocatalyst. Figure 5d shows the fine spectrum of Mo 3d. The two peaks located at 228.7 and 232.1 eV correspond to the Mo $3d_{5/2}$ and Mo $3d_{3/2}$ orbitals and are attributed to Mo^{4+} in 1T-MoS_2 . The peaks located at 229.5 and 233.1 eV correspond to Mo^{4+} in 2H-MoS_2 and are about 1 eV higher than the binding energy of 1T-MoS_2 .¹⁹ The presence of a peak belonging to Mo^{6+} located at 236 eV may be due to the incomplete reaction of MoO_3 or incomplete removal during washing, which is consistent with the XRD

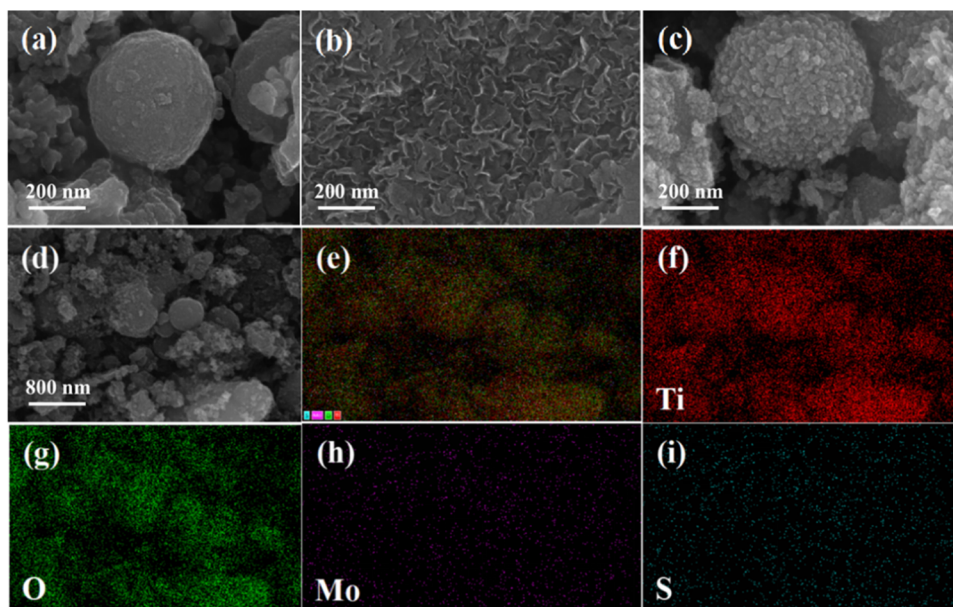


Figure 3. (a–c) SEM images of TiO_2 , 1T/2H- MoS_2 , and 1T/2H- $\text{MoS}_2/\text{TiO}_2$. (d–i) EDS elemental distribution of Mo, S, Ti, and O for 1T/2H- $\text{MoS}_2/\text{TiO}_2$.

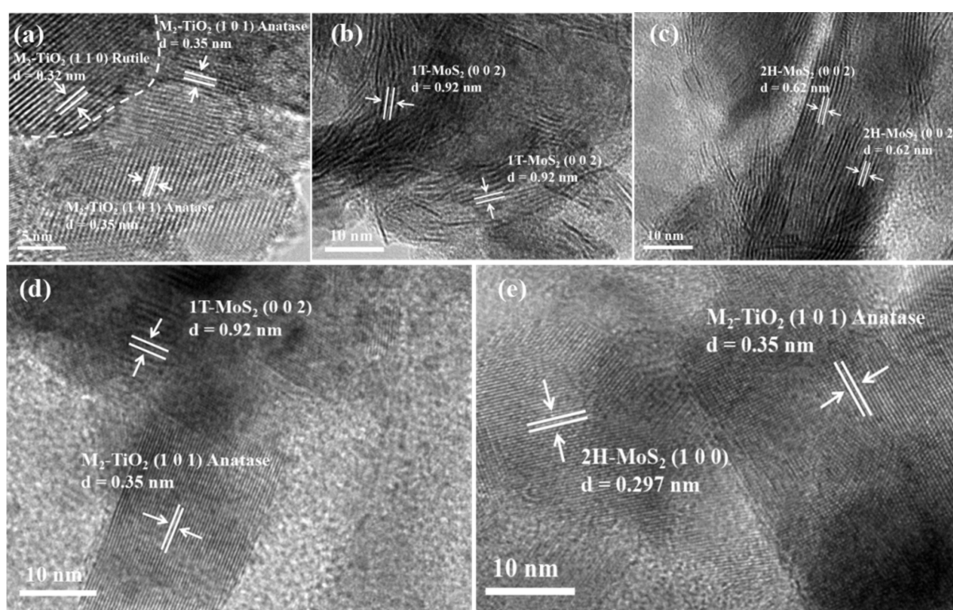


Figure 4. (a) High-resolution TEM image of TiO_2 . (b, c) High-resolution TEM images of 1T/2H- MoS_2 . (d, e) High-resolution TEM images of 1T/2H- $\text{MoS}_2/\text{TiO}_2$.

results. Figure 5e shows the fine pattern of S 2p, with two peaks at 161.4 and 162.8 eV corresponding to the S $2p_{3/2}$ and S $2p_{1/2}$ orbitals of 1T- MoS_2 . The peaks at 161.9 and 163.2 eV correspond to the S $2p_{3/2}$ and S $2p_{1/2}$ orbitals of 2H- MoS_2 , both of which can be attributed to S^{2-} . All these results further demonstrate the successful preparation of T/2H- $\text{MoS}_2/\text{TiO}_2$, and the original crystalline structures of TiO_2 and 1T/2H- MoS_2 were not affected.

The photoresponse range of the catalyst is one of the important factors affecting the photocatalytic effect. Figure 6a shows the UV–vis absorption spectra of TiO_2 , 1T/2H- MoS_2 , and 1T/2H- $\text{MoS}_2/\text{TiO}_2$. It can be seen from the figure that TiO_2 mainly absorbs light less than 400 nm. 1T/2H- MoS_2 has almost no absorption edge because of the presence of the 1T

phase, which has metal-like properties. The 1T/2H- $\text{MoS}_2/\text{TiO}_2$ composite photocatalyst has a similar absorption spectral trend to TiO_2 , but with an increase in intensity in the range greater than 400 nm. The forbidden bandwidths of 1T/2H- MoS_2 , TiO_2 , and 1T/2H- $\text{MoS}_2/\text{TiO}_2$ are obtained from the Tauc formula and are shown in Figure 6b. The forbidden bandwidths were 3.22 eV for TiO_2 , 1.33 eV for 1T/2H- MoS_2 , 3.18 eV for 1T/2H- $\text{MoS}_2/\text{TiO}_2$ -3wt %, and 3.11 eV for 1T/2H- $\text{MoS}_2/\text{TiO}_2$ -10wt %, indicating that the forbidden bandwidth of the composites formed by 1T/2H- MoS_2 and TiO_2 became narrower than that of TiO_2 , and the narrower forbidden bandwidth made the catalysts easier to be excited, resulting in a better photocatalytic effect.

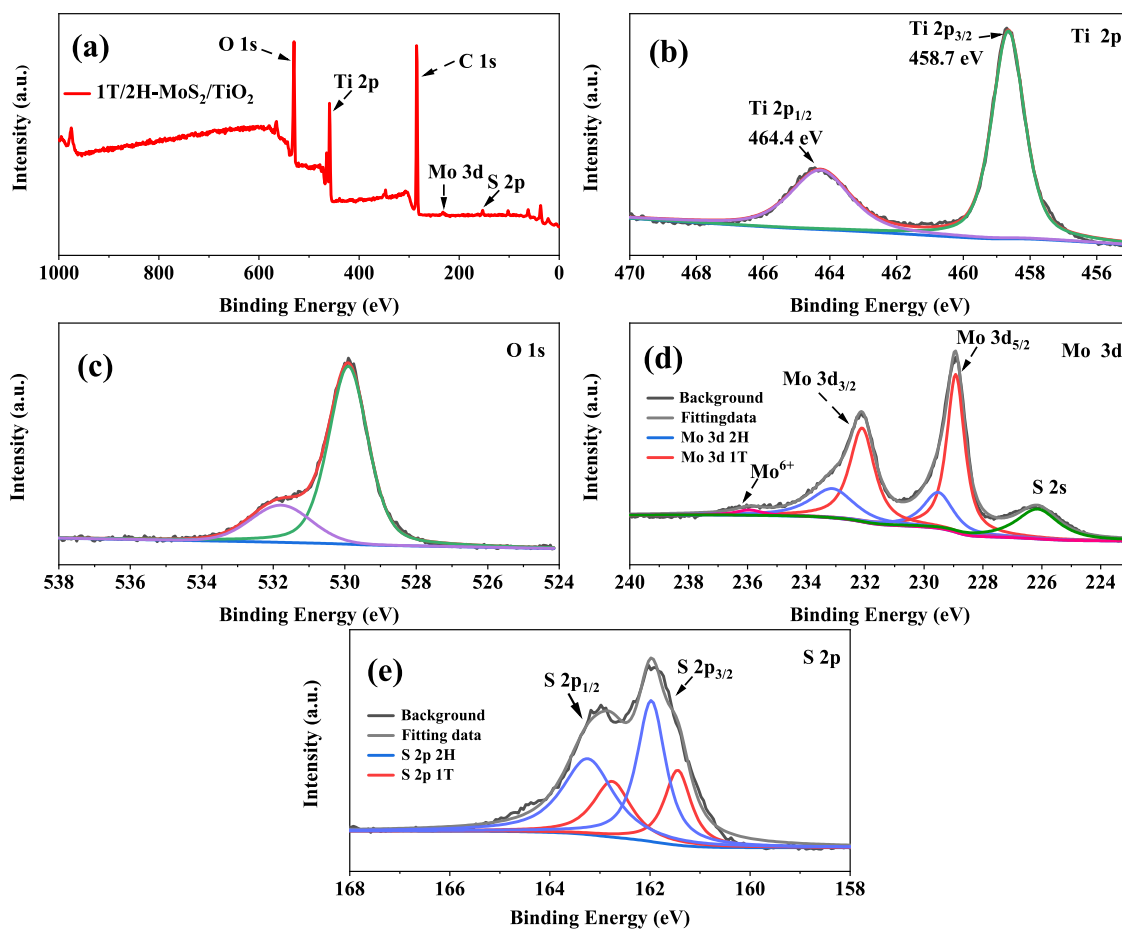


Figure 5. (a) XPS full spectrum of 1T/2H-MoS₂/TiO₂. XPS fine spectra of (b) Ti 2p, (c) O 1s, (d) Mo 3d, and (e) S 2p of 1T/2H-MoS₂/TiO₂.

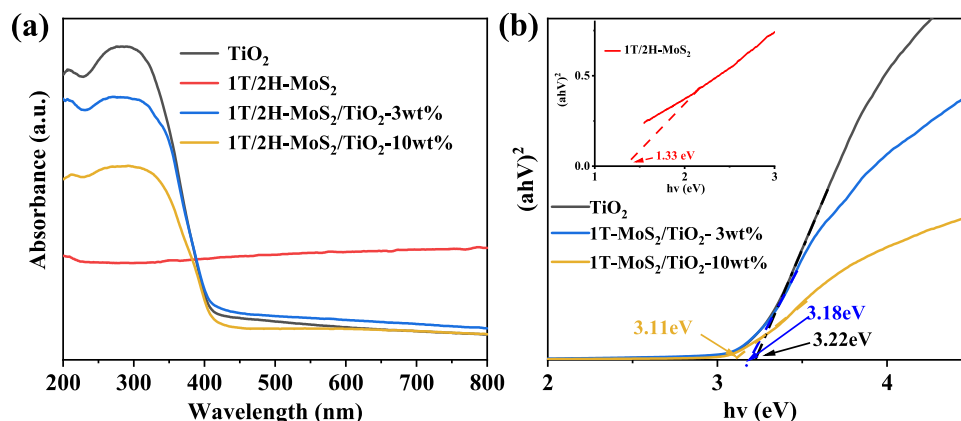


Figure 6. (a) UV-vis absorption spectra of TiO₂, 1T/2H-MoS₂, 1T/2H-MoS₂/TiO₂-3wt %, and 1T/2H-MoS₂/TiO₂-10wt %. (b) Forbidden bandwidths of TiO₂, 1T/2H-MoS₂, 1T/2H-MoS₂/TiO₂-3wt %, and 1T/2H-MoS₂/TiO₂-10wt %.

The degradation ability of the prepared photocatalysts was examined using TC-HCl as the target pollutant. Figure 7a shows the graphs of the degradation of TC-HCl under the same conditions for TiO₂, 1T/2H-MoS₂, and different ratios of 1T/2H-MoS₂/TiO₂. The degradation effect of 1T/2H-MoS₂/TiO₂ was the worst, with only 2% degradation after 1 h of visible-light irradiation, which was almost negligible, and TiO₂ degraded about 20.9% of TC-HCl after 1 h. The degradation effect of any ratio of 1T/2H-MoS₂/TiO₂ composite photocatalyst was better than that of the single 1T/2H-MoS₂ and TiO₂, and the degradation effect was related to the mass ratio

of 1T/2H-MoS₂ and TiO₂, and the degradation efficiency showed an increasing and then decreasing trend with the increasing loading of 1T/2H-MoS₂, which might be due to the fact that excessive loading of 1T/2H-MoS₂ would instead cover the active sites on the photocatalyst surface and affect the photocatalytic degradation effect. The degradation of TC-HCl by all the photocatalysts was in accordance with the first-order kinetic equation. Figure 7b shows the first-order kinetic fitting curves of 1T/2H-MoS₂, TiO₂, and 1T/2H-MoS₂/TiO₂-3wt % with rate constants of 2.41×10^{-4} , 1.71×10^{-3} , and 7.02×10^{-3} , respectively, and the reaction rates of 1T/2H-

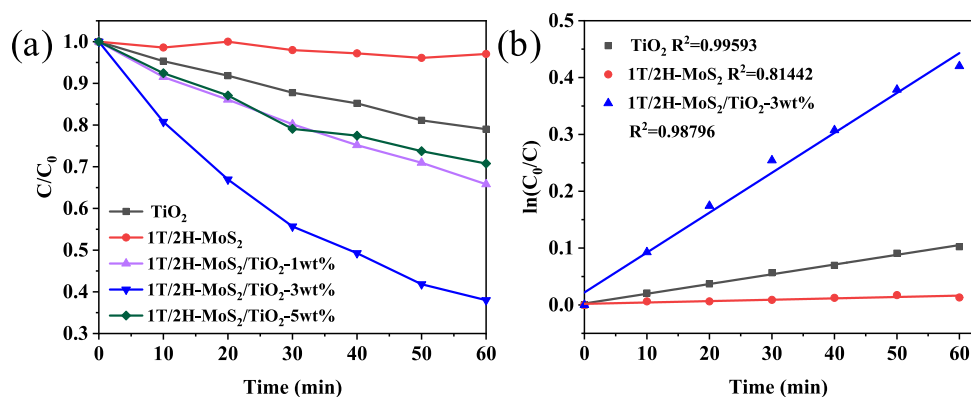


Figure 7. (a) TiO_2 , 1T/2H- MoS_2 , and different ratios of the 1T/2H- $\text{MoS}_2/\text{TiO}_2$ -catalyzed degradation of TC-HCl under visible-light curves. (b) First-order kinetic fitting curves of TiO_2 , 1T/2H- MoS_2 , and 1T/2H- $\text{MoS}_2/\text{TiO}_2$ -3wt %.

$\text{MoS}_2/\text{TiO}_2$ -3wt % were 29 and 4 times higher than those of 1T/2H- MoS_2 and TiO_2 , respectively.

HPLC was used to monitor whether the byproducts or intermediates were formed during the photocatalytic degradation of 1T/2H- $\text{MoS}_2/\text{TiO}_2$. The test results are shown in Figure 8, which shows that the peak of TC-HCl gradually

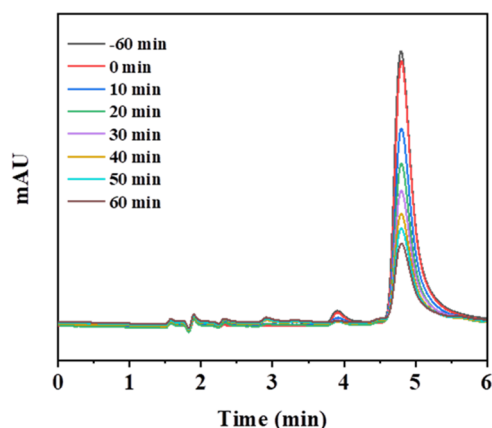


Figure 8. HPLC of the 1T/2H- $\text{MoS}_2/\text{TiO}_2$ -3wt % degradation of TC-HCl.

decreased with the reaction time, proving that TC-HCl was gradually mineralized. In addition, no other peaks appeared during the reaction, proving that no byproducts or intermediates were generated during the degradation of TC-HCl.

The cycling stability of a photocatalyst is one of the most important indicators of its performance. Fifty milligrams of 1T/2H- $\text{MoS}_2/\text{TiO}_2$ -3wt % was subjected to five cycles of stability experiments, and the experimental results are shown in Figure 9. The degradation effect of 1T/2H- $\text{MoS}_2/\text{TiO}_2$ -3wt % could reach 68.1% at the end of the first cycle, and the degradation effect could still be maintained at 66.0% after the second cycle, which is not a great change. However, the degradation effect after the third cycle was 53.5%, which was a big change compared with the results of the first two cycles. It can also be seen from the graph that the degradation effect gradually stabilized from the third cycle to the fifth cycle, and the degradation effect was maintained at 43.0% after the fifth cycle. The significant decrease in the degradation rate in the third cycle may be due to the loss of catalyst in the process of this cycle.

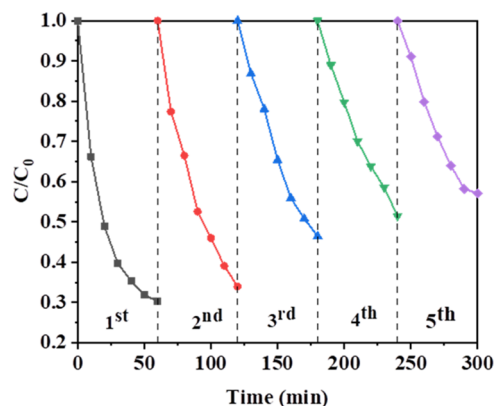


Figure 9. Cycling stability test of the 1T/2H- $\text{MoS}_2/\text{TiO}_2$ -3wt % degradation of tetracycline hydrochloride.

To examine the charge transfer capability of 1T/2H- $\text{MoS}_2/\text{TiO}_2$, a photocurrent test was carried out. Figure 10a shows the transient photocurrent test curves of 1T/2H- MoS_2 , TiO_2 , and 1T/2H- $\text{MoS}_2/\text{TiO}_2$, in which it can be seen that the response intensity of 1T/2H- $\text{MoS}_2/\text{TiO}_2$ to visible light is significantly greater than that of 1T/2H- MoS_2 and TiO_2 , and the enhanced photocurrent response can be attributed to the good charge transfer capability of 1T/2H- MoS_2 and the enhanced charge separation efficiency of the heterojunction. The enhanced photocurrent response can be attributed to the good charge transport ability of 1T/2H- MoS_2 and the enhanced charge separation efficiency of the heterojunction, which may also be one of the reasons for the better photocatalytic activity of 1T/2H- $\text{MoS}_2/\text{TiO}_2$. Figure 10b shows the impedance plots of 1T/2H- MoS_2 , TiO_2 , and 1T/2H- $\text{MoS}_2/\text{TiO}_2$, in which it can be seen that the EIS arc radius of 1T/2H- MoS_2 is smaller than the EIS arc radius of TiO_2 , indicating that the resistance of the 1T/2H- $\text{MoS}_2/\text{TiO}_2$ composite is significantly reduced compared to that of TiO_2 . And the smaller resistance is beneficial to the charge transfer.

The active substance of 1T/2H- $\text{MoS}_2/\text{TiO}_2$ in photocatalytic reactions was investigated by capture experiments. TBA, EDTA, and BQ were added to the aqueous TC-HCl solution to capture the $-\text{OH}$, h^+ , and $-\text{O}_2^-$ produced during the photocatalytic process, respectively. From Figure 11a, it can be seen that EDTA and BQ have a greater effect on the photocatalytic degradation effect, while TBA has basically no effect on the photocatalytic degradation effect, which proves

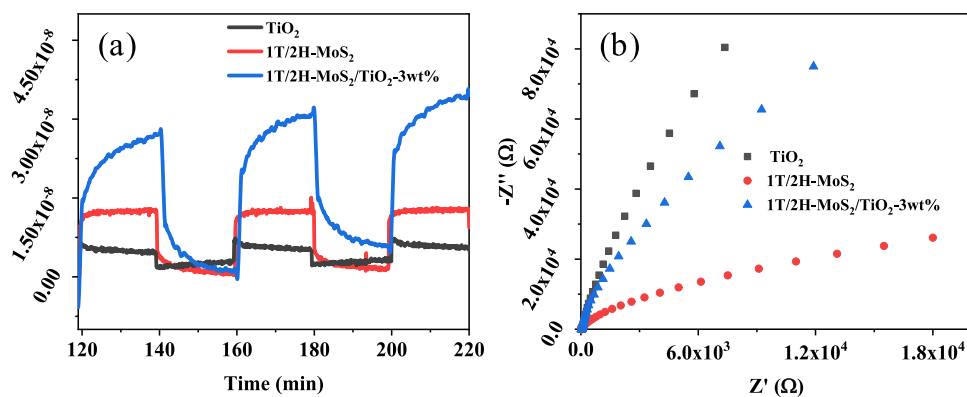


Figure 10. (a) Transient photocurrent response test curves for TiO₂, 1T/2H-MoS₂, and 1T/2H-MoS₂/TiO₂-3wt%. (b) Impedance of TiO₂, 1T/2H-MoS₂, and 1T/2H-MoS₂/TiO₂-3wt%.

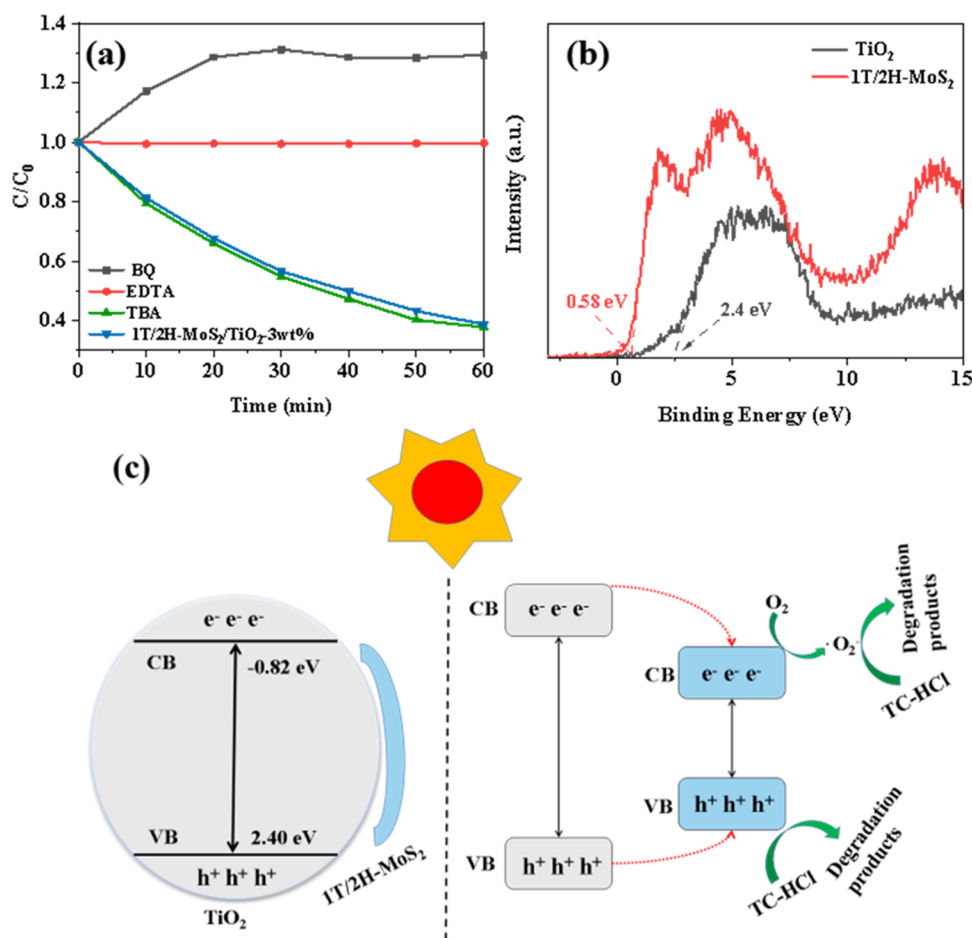


Figure 11. (a) Capture experiment of 1T/2H-MoS₂/TiO₂-3wt%. (b) XPS valence band spectra of 1T/2H-MoS₂ and TiO₂. (c) Photocatalytic mechanism diagram of 1T/2H-MoS₂/TiO₂-3wt%.

that h^+ and $-O_2^-$ are the main active substances in the degradation of TC-HCl by 1T/2H-MoS₂/TiO₂.

In order to determine the conduction band and valence band positions of 1T/2H-MoS₂ and TiO₂, the valence band spectra of both were obtained by XPS test, as shown in Figure 11b, and the valence band positions of both were 0.58 and 2.4 eV, respectively. Combining the above data, the photocatalytic mechanism of 1T/2H-MoS₂/TiO₂ was finally obtained, as shown in Figure 11c. Under solar light irradiations, TiO₂ mesoporous beads absorb the UV light, making electrons excite from their valence band (VB) to their conduction band

(CB). Hybridized 1T/2H-MoS₂ absorbs light in the visible region, promoting electrons from their VB to their CB. The light absorption of both materials therefore generates electron–hole pairs.²⁹ When 1T/2H-MoS₂ and TiO₂ are excited by light irradiation, e^- jumps from the valence band to the conduction band, generating photogenerated electrons while leaving photogenerated h^+ in the valence band. Since the conduction band and the valence band of 1T/2H-MoS₂ are located between the conduction band and the valence band of TiO₂, they form a typical type I heterojunction. e^- and h^+ in the conduction band and valence band of TiO₂ are transferred

to the conduction band and valence band of 1T/2H-MoS₂, respectively. Therefore, the reduction reaction will first occur in the conduction band of 1T/2H-MoS₂. e⁻ will reduce O₂ to -O₂⁻ and -O₂⁻ will continue to react with TC-HCl to mineralize it. 1T/2H-MoS₂ does not meet the conditions for the formation of -OH in the valence band, so h⁺ will. This conclusion is also supported by the capture experiment.

4. CONCLUSIONS

In summary, anatase-rutile mixed-phase TiO₂ was prepared in this paper, and then 1T/2H-MoS₂/TiO₂ composite photocatalyst was prepared with 1T/2H-MoS₂, which is expected to replace noble metals. Compared with TiO₂ and 1T/2H-MoS₂, the 1T/2H-MoS₂/TiO₂ composite has better photocurrent response efficiency and electron-hole separation efficiency. 1T/2H-MoS₂/TiO₂ exhibits better photocatalytic performance and better stability in the visible-light degradation of TC-HCl, which may have a good application prospect in the treatment of organic pollutants in water.

AUTHOR INFORMATION

Corresponding Authors

Miaogen Chen – Key Laboratory of Intelligent Manufacturing Quality Big Data Tracing and Analysis of Zhejiang Province, College of Science, China Jiliang University, Hangzhou 310018, China; orcid.org/0000-0003-1930-8331; Email: phycmg@163.com

Zhi Chen – College of Materials and Chemistry, China Jiliang University, Hangzhou 310018, China; orcid.org/0000-0002-5973-8910; Email: zchen@cjlu.edu.cn

Authors

Wenya Chang – Key Laboratory of Intelligent Manufacturing Quality Big Data Tracing and Analysis of Zhejiang Province, College of Science, China Jiliang University, Hangzhou 310018, China

Jing Zhang – Key Laboratory of Intelligent Manufacturing Quality Big Data Tracing and Analysis of Zhejiang Province, College of Science, China Jiliang University, Hangzhou 310018, China; orcid.org/0009-0000-2880-5159

Wan Zhao – College of Materials and Chemistry, China Jiliang University, Hangzhou 310018, China

Complete contact information is available at:
<https://pubs.acs.org/10.1021/acsomega.3c00730>

Notes

The authors declare no competing financial interest.

ACKNOWLEDGMENTS

This work was financially supported by the National Key R&D Program of China (2019YFE0112000), the Fundamental Research Funds for the Provincial Universities of Zhejiang (2021YW25), and the Scientific Research Fund of Zhejiang Provincial Education Department (Y202249403).

REFERENCES

- (1) Yang, X.; Chen, Z.; Zhao, W.; Liu, C.; Qian, X.; Zhang, M.; Wei, G.; Khan, E.; Hau Ng, Y.; Sik Ok, Y. Recent advances in photodegradation of antibiotic residues in water. *Chem. Eng. J.* **2021**, *405*, No. 126806.
- (2) Tayade, R. J.; Gandhi, V. *Photocatalytic Nanomaterials for Environmental Applications*; Materials Research Forum LLC: Millersville, PA, 2018; pp 139–167.

- (3) Varma, K. S.; Tayade, R. J.; Shah, K. J.; Joshi, P. A.; Shukla, A. D.; Gandhi, V. G. Photocatalytic degradation of pharmaceutical and pesticide compounds (PPCs) using doped TiO₂ nanomaterials: A review. *Water-Energy Nexus* **2020**, *3*, 46–61.

- (4) Noman, M. T.; Ashraf, M. A.; Ali, A. Synthesis and applications of nano-TiO₂: a review. *Environ. Sci. Pollut. Res.* **2019**, *26*, 3262–3291.

- (5) Ahmed, S. N.; Haider, W. Heterogeneous photocatalysis and its potential applications in water and wastewater treatment: a review. *Nanotechnology* **2018**, *29*, No. 342001.

- (6) Isaifan, R. J.; Samara, A.; Suwaileh, W.; Johnson, D.; Yiming, W.; Abdallah, A. A.; Aissa, B. Improved Self-cleaning Properties of an Efficient and Easy to Scale up TiO₂ Thin Films Prepared by Adsorptive Self-Assembly. *Sci. Rep.* **2017**, *7*, No. 9466.

- (7) Zhang, P.; Zhang, L.; Kang, Y.; He, B.; Zhao, Z.; Hung, C.; Duan, L.; Chen, W.; Tang, Y.; Yu, J.; Mai, L.; Li, Y.; Li, W.; Zhao, D. Sub-10 nm Corrugated TiO₂ Nanowire Arrays by Monocell-Directed Assembly for Efficient Hole Extraction. *J. Am. Chem. Soc.* **2022**, *144*, 20964.

- (8) Tong, H.; Ouyang, S.; Bi, Y.; Umezawa, N.; Oshikiri, M.; Ye, J. Nano-photocatalytic Materials: Possibilities and Challenges. *Adv. Mater.* **2012**, *24*, 229–251.

- (9) Singh, R.; Dutta, S. A review on H₂ production through photocatalytic reactions using TiO₂/TiO₂-assisted catalysts. *Fuel* **2018**, *220*, 607–620.

- (10) Humayun, M.; Raziq, F.; Khan, A.; Luo, W. Modification strategies of TiO₂ for potential applications in photocatalysis: a critical review. *Green Chem. Lett. Rev.* **2018**, *11*, 86–102.

- (11) Liang, Z.; Shen, R.; Ng, Y. H.; Zhang, P.; Xiang, Q.; Li, X. A review on 2D MoS₂ cocatalysts in photocatalytic H₂ production. *J. Mater. Sci. Technol.* **2020**, *56*, 89–121.

- (12) Eda, G.; Fujita, T.; Yamaguchi, H.; Voiry, D.; Chen, M.; Chhowalla, M. Coherent atomic and electronic heterostructures of single-layer MoS₂. *ACS Nano* **2012**, *6*, 7311.

- (13) Wang, Q. H.; Kalantar-Zadeh, K.; Kis, A.; Coleman, J. N.; Strano, M. S. Electronics and optoelectronics of two-dimensional transition metal dichalcogenides. *Nat. Nanotechnol.* **2012**, *7*, 699–712.

- (14) Jayabal, S.; Wu, J.; Chen, J.; Geng, D.; Meng, X. Metallic 1T-MoS₂ nanosheets and their composite materials: Preparation, properties and emerging applications. *Mater. Today Energy* **2018**, *10*, 264–279.

- (15) Lukowski, M. A.; Daniel, A. S.; Meng, F.; Forticaux, A.; Li, L.; Jin, S. Enhanced hydrogen evolution catalysis from chemically exfoliated metallic MoS₂ nanosheets. *J. Am. Chem. Soc.* **2013**, *135*, 10274–10277.

- (16) Han, H.; Kim, K. M.; Lee, C. W.; Lee, C. S.; Pawar, R. C.; Jones, J. L.; Hong, Y. R.; Ryu, J. H.; Song, T.; Kang, S. H.; Choi, H.; Mhin, S. Few-layered metallic 1T-MoS₂/TiO₂ with exposed (001) facets: two-dimensional nanocomposites for enhanced photocatalytic activities. *Phys. Chem. Chem. Phys.* **2017**, *19*, 28207–28215.

- (17) Bai, S.; Wang, L.; Chen, X.; Du, J.; Xiong, Y. Chemically exfoliated metallic MoS₂ nanosheets: a promising supporting cocatalyst for enhancing the photocatalytic performance of TiO₂ nanocrystals. *Nano Res.* **2015**, *8*, 175–183.

- (18) Xu, X.; Zhou, G.; Dong, X.; Hu, J. Interface Band Engineering Charge Transfer for 3D MoS₂ Photoanode to Boost Photoelectrochemical Water Splitting. *ACS Sustainable Chem. Eng.* **2017**, *5*, 3829–3836.

- (19) Zhao, W.; Liu, X.; Yang, X.; Liu, C.; Qian, X.; Sun, T.; Chang, W.; Zhang, J.; Chen, Z. Synthesis of Novel 1T/2H-MoS₂ from MoO₃ Nanowires with Enhanced Photocatalytic Performance. *Nanomaterials* **2020**, *10*, 1124.

- (20) Geng, X.; Sun, W.; Wu, W.; Chen, B.; Al-Hilo, A.; Benamara, M.; Zhu, H.; Watanabe, F.; Cui, J.; Chen, T.-P. Pure and stable metallic phase molybdenum disulfide nanosheets for hydrogen evolution reaction. *Nat. Commun.* **2016**, *7*, No. 10672.

- (21) Hu, X.; Zeng, X.; Liu, Y.; Lu, J.; Yuan, S.; Yin, Y.; Hu, J.; McCarthy, D. T.; Zhang, X. Nano-layer based 1T-rich MoS₂/g-C₃N₄ co-catalyst system for enhanced photocatalytic and photoelectrochemical activity. *Appl. Catal., B* **2020**, *268*, No. 118466.

- (22) Shi, S.; Sun, Z.; Hu, Y. H. Synthesis, stabilization and applications of 2-dimensional 1T metallic MoS₂. *J. Mater. Chem. A* **2018**, *6*, 23932–23977.
- (23) Bai, S.; Wang, L.; Chen, X.; Du, J.; Xiong, Y. Chemically exfoliated metallic MoS₂ nanosheets: A promising supporting cocatalyst for enhancing the photocatalytic performance of TiO₂ nanocrystals. *Nano Res.* **2015**, *8*, 175–183.
- (24) Wang, M.; Zhang, H.; Zu, H.; Zhang, Z.; Han, J. Construction of TiO₂/CdS heterojunction photocatalysts with enhanced visible light activity. *Appl. Surf. Sci.* **2018**, *455*, 729–735.
- (25) Zhao, W.; Yang, X.; Liu, C.; Qian, X.; Wen, Y.; Yang, Q.; Sun, T.; Chang, W.; Liu, X.; Chen, Z. Facile Construction of All-Solid-State Z-Scheme g-C₃N₄/TiO₂ Thin Film for the Efficient Visible-Light Degradation of Organic Pollutant. *Nanomaterials* **2020**, *10*, No. 600.
- (26) Lan, K.; Wang, R.; Zhang, W.; Zhao, Z.; Elzatahry, A.; Zhang, X.; Liu, Y.; Al-Dhayan, D.; Xia, Y.; Zhao, D. Mesoporous TiO₂ Microspheres with Precisely Controlled Crystallites and Architectures. *Chem* **2018**, *4*, 2436–2450.
- (27) Zhang, W.; He, H.; Tian, Y.; Lan, K.; Liu, Q.; Wang, C.; Liu, Y.; Elzatahry, A.; Che, R.; Li, W.; Zhao, D. Synthesis of uniform ordered mesoporous TiO₂ microspheres with controllable phase junctions for efficient solar water splitting. *Chem. Sci.* **2019**, *10*, 1664–1670.
- (28) Su, J.; Yu, S.; Xu, M.; Guo, Y.; Sun, X.; Fan, Y.; Zhang, Z.; Yan, J.; Zhao, W. Enhanced visible light photocatalytic performances of few-layer MoS₂@TiO₂ hollow spheres heterostructures. *Mater. Res. Bull.* **2020**, *130*, No. 110936.
- (29) Alido, J. P. M.; Sari, F. N. I.; Ting, J.-M. Synthesis of Ag/hybridized 1T-2H MoS₂/TiO₂ heterostructure for enhanced visible-light photocatalytic activity. *Ceram. Int.* **2019**, *45*, 23651–23657.